fractal and fractional

MDPI

Article

A New Fractional Boundary Element Model for Anomalous Thermal Stress Effects on Cement-Based Materials

Mohamed Abdelsabour Fahmy [1,2] and Roqia Abdullah A. Jeli [3,*]

[1] Department of Mathematics, Adham University College, Umm Al-Qura University, Adham, Makkah 28653, Saudi Arabia; maselim@uqu.edu.sa
[2] Department of Basic Sciences, Faculty of Computers and Informatics, Suez Canal University, New Campus, Ismailia 41522, Egypt
[3] Department of Mathematics, Faculty of Science, Jazan University, Jazan 45142, Saudi Arabia
* Correspondence: rjeli@jazanu.edu.sa; Tel.: +966-544377378

Abstract: The novelty of this work is the development of a new fractional boundary element model based on the Caputo derivative to investigate anomalous thermal stress effects on cement-based materials. To obtain the BEM integral equations for the proposed formulation, we employ the weighted residuals technique, with the anisotropic fundamental solution serving as the weighting function in the anomalous heat governing equation. The Caputo fractional derivative was employed as an integrand for the domain integral of the proposed formulation. The time step selection is less dependent on the time derivative order. This allows the approach to overcome the non-locality of the fractional operators. The key benefit provided by the suggested formulation is the ability to analyze situations with tiny values of the fractional time derivative. The current BEM methodology proves that it is a useful tool for solving fractional calculus problems.

Keywords: fractional order; Caputo derivative; boundary element method; anomalous thermal stresses; cement-based materials

Citation: Fahmy, M.A.; Jeli, R.A.A. A New Fractional Boundary Element Model for Anomalous Thermal Stress Effects on Cement-Based Materials. *Fractal Fract.* **2024**, *8*, 753. https://doi.org/10.3390/fractalfract8120753

Academic Editors: Ervin K. Lenzi and Aloisi Somer

Received: 22 November 2024
Revised: 18 December 2024
Accepted: 19 December 2024
Published: 21 December 2024

1. Introduction

Over the last few decades, there has been growing interest in investigating anomalous heat transmission in various materials. Anomalous behavior is frequently defined by a power-law spatial fall in temperature within a homogeneous medium, where the heat equation may be used [1–3]. In many complex media, the heat equation may not be applicable; thus, the parabolic equation governing heat diffusion can be replaced with a broader view. For example, fractional differential heat diffusion equations have been derived for numerous materials incorporating mass fractals. Some media with spatial non-local behaviors, fractional derivative features, and non-conserving energy may show a non-local temporal rate of change in the thermal stress tensor [4–7].

Cement-based materials, also known as porous composites, have been widely used in a range of constructions due to their technical, mechanical, and chemical qualities. Moisture transport has been widely established to have an impact on the service performance and life of cement-based materials [8,9]. Because of their variety and complexity, cement-based materials exhibit more anomalous moisture transport characteristics than other porous materials [10–13]. Moisture transport systems and moisture distribution exhibit various anomalous properties in distinct ways. The accessibility of bulk liquid water within the material, indicating linear passage in the pore space, is measured over time [14–16]. Fick's second law describes an ordinary diffusion mechanism that accounts for mass continuity. It has been widely utilized to determine the liquid or vapor transfer of moisture in cement-based materials. The study indicated that the Fickian model provides a solid foundation for predicting the lifespan of cement-based materials by fitting vapor transport measurement

data [17–19]. Bridges, walkways, slabs, pavements, floors, and walls are among the structural and prefabricated components constructed with cement-based materials. Concrete is also utilized to construct storage tanks, swimming pools, subterranean parking lots, and other structures. Because of climate change, numerous of these elements are constantly subjected to temperature fluctuations. These fluctuations result in temperature gradients, which produce internal tensions in the substance. Depending on how the temperature changes, these forces may cause cracking [20–22].

It is well recognized that thermally generated stresses in concrete can cause serious problems. These stresses have the potential to fracture or spall concrete due to its low tensile strength. Although this happens frequently in pavement, temperature gradients and other boundary circumstances make it more frequent in structural concrete. However, practicing engineers may not fully comprehend the phenomenon of thermal stresses and their possible effects on concrete structures [23]. They may think that the lack of a temperature gradient or other type of temperature difference in a structure is sufficient to stop thermal stresses from developing, and as a result, the stresses should be disregarded. They ignore how aging affects the material properties of concrete, including creep, shrinkage, and heat production from hydration [24–26].

There are more physical mechanisms for strains to originate in concrete. Because concrete is hot wrought by nature, it lacks a faultless structure free of flaws. When exposed to a thermal environment, each component of the concrete has a different temperature, and when it warms or cools, the concrete creates internal strains. After that, the strength drops, and quick heating can result in extremely high-tension stress in the concrete [27,28]. Tensile stress is an important design consideration for nuclear reactor containment structures because they can become extremely fragile at high temperatures. Therefore, it is vital to design a structure so that the maximum stress does not exceed the material's tensile strength. The proper application of admixtures can improve the concrete's durability to high temperatures; nevertheless, this is heavily dependent on the concrete's underlying structure. It has long been recognized that stress development and heat transfer are important aspects in the risk assessment and quality analysis of concrete structures exposed to a variety of temperature histories. Aside from thermal expansion and plain concrete cracking, other current concerns include temperature effects on interactions between multiple structural members or systems, the combination of mechanical load and hostile environment, dangerous interactions between transported hazardous materials, and temperature histories that are either time-dependent or irreversible. To assess the thermal stress related to encapsulating hazardous waste forms, exact temperature gradients must be identified. The temperature history also indicates that concrete exposed to high temperatures may degrade [29–32]. Concrete is a ceramic material composed mostly of cement, water, and coarse and fine particles. When a concrete structure is exposed to temperature changes, cement-based materials may not react uniformly, resulting in axial strains and thermal gradients [33,34]. These non-uniform responses cause internal stresses of varying magnitudes, compromising the specimen's integrity. These generated stresses can threaten the concrete's serviceability or be used to create fracture-mitigation solutions. Understanding and preventing crack propagation necessitates a detailed understanding of heat gradient effects on cement-based materials [35].

The primary causes of thermal stresses in cement-based materials are inhomogeneous thermal expansion and inhomogeneous cooling or heating. Inhomogeneous thermal expansion occurs when the heat exchange between the parts of the structure and the environment, or between different parts of the structure, is very different, or when the strength or viscoelastic properties of the materials or the structure under temperature load differ greatly. During the cooling process, structural elements whose behavior changes between temperatures, from temperature softening to temperature hardening, behave similarly to elements with a positive coefficient of temperature expansion, and cooling causes compressive stresses in the interior of the affected parts of the structure. Inhomogeneous heating is most common when infrared radiators are initially utilized to heat the concrete or formwork

parts. In this situation, the surface elements of the concrete, or at least the cores of the formwork parts, are rapidly heated, while the rest of the elements remain virtually cold. In the second instance, the heating of the entire structure occurs uniformly. Due to possible consultations, the temperature load changes from homogenous to inhomogeneous. The development of temperature load and tensile strains on the surface of the heated elements is depicted schematically. During the initial heating stage, the surface layer may be so constrained that as the temperature differential between the various components rises, tensile tensions develop on more than simply the surface. This effect is very likely in temperature-hardening materials, but it can also happen if interesting thermal processes occur in temperature-prevailing materials during concrete casting [36].

The development of thermal strains in cement-based materials, such as concrete and mortar, is a common challenge for material designers and practicing engineers. This problem is widely understood in simple engineering terms, as the essential conditions required for the generation of bulk thermal stresses have long been recognized. Everyone understands that if one side of a ceramic disk is heated while the other face remains cool, the disk will be unable to expand, and if constrained, it will exert significant force on its supports. The relevance of the development of thermal stresses varies greatly depending on the distribution of a concrete element. Thermal deformations in small elements will be modest, and the associated stresses will be relatively minor, assuming that the designer was aware of the anticipated order of magnitude of the stresses and provided concrete of sufficient strength. Thermal pressures can have a significant impact on highway bridges. In these instances, a fast rise in temperature may cause stresses that may only be assessed over short time periods [37].

Research into fractional boundary element models for anomalous thermal stress has advanced significantly, resulting in a more nuanced knowledge of how fractional calculus can be applied to complex thermal phenomena. Ceretani's work [38] focuses on time-fractional free boundary concerns of the Stefan type, highlighting the significance of using appropriate fractional models to accurately depict physical processes, particularly anomalous phase transitions. According to Ceretani [38], classical conservation equations may not be consistent with non-local constitutive equations, implying that the complexities of fractional derivatives must be carefully examined when modeling events such as phase transitions. This initial study lays the groundwork for a more comprehensive examination of fractional techniques in thermal stress analysis. Patnaik et al. [39] extend the approach to incorporate non-local elasticity, utilizing fractional order to study non-local models.

The Boundary Element Method (BEM) has developed into an effective numerical method that is now recognized as belonging to the broad category of numerical methods designed to examine continuum mechanics problems [40–42]. BEM is intriguing because it allows for the introduction of unlimited domains while requiring only boundary information for mathematical representation. For these reasons, BEM is ideal for evaluating fields in unbounded regions [43,44]. The method generates dependable numerical results that are extensive and accurate, while using only a few field samples from the region of interest [45–49]. Over the last three decades, BEM applications have grown beyond their original appeal in the static linear elasticity field. Currently, BEM is an appealing, efficient, and sophisticated tool for simulating a wide range of problems. The method's dependability stems from its primary quality of simulating nature at the physical level of consideration by employing precise mathematical equations of continuum deformation. The subjects covered in this issue provide a cross-section of BEM activity areas and may be useful to readers interested in various BEM features and applications [50–52].

The anomalous heat conduction equation has lately acquired prominence due to its realistic uses in modeling diverse insulators and semiconductors, ultrashort pulse phenomena, linear scaling of multi-layer porous silicon, and the rapid heat dissipation rates of aromatic copper chain complexes. The anomalous heat conduction equation's main feature is its dynamical self-similarity, which results from the fact that the length scale of the heat conduction behavior is essentially quantum mechanical and does not break down

into any shorter lengths. The boundary element approach was created to solve thermal stress problems but not anomalous thermal stress problems [53].

In this research, we provide a new two-dimensional boundary element approach framework that shows the increasing recognition of fractional calculus as a significant tool for understanding and modeling anomalous thermal stress problems in cement-based materials. A novel two-dimensional boundary element approach framework that demonstrates the growing recognition of fractional calculus as an important tool for understanding and modeling anomalous thermal stress problems in cement-based materials, revealing both theoretical advances and practical implications in a variety of fields. The suggested formulation's boundary integral equation is derived using a weighted residual approach, with the anisotropic fundamental solution serving as the weighting function in the presence of a domain integral, including the Caputo derivative. It may characterize the non-local behavior of the thermal stress tensor in space as well as the rate of change over time from a thermodynamically compatible perspective. Comparisons of model responses to experimentally observed thermal stress behaviors in several types of cement composites demonstrate good agreement across the range of interest. The model's physical parameters, which are determined by the materials' basic thermomechanical properties, also exhibit fractal-like behavior. The given model could be applied to the thermal stress analysis of various complex materials exhibiting non-local effects.

2. Formulation of the Problem

The fractional anomalous thermal stress governing equations for anisotropic cement-based materials are as follows [53,54]:

$$\sigma_{ij,j} = \rho \ddot{u}_i + \phi \rho_{\mathcal{F}} \ddot{v}_i \tag{1}$$

$$\dot{\zeta} + q_{i,i} = \overline{\mathbb{C}} \tag{2}$$

$$\frac{\partial_C^a T}{\partial \tau^a} = D_{x_1} \frac{\partial^2 T}{\partial x_1^2} + \frac{\partial^2 T}{\partial x_2^2} D_{x_2}, \;\; 0 < a < 1 \tag{3}$$

where

$$\sigma_{ij} = C_{ijkl}\, e\delta_{ij} - A\delta_{ij} p - \beta_{ij}\, T \tag{4}$$

$$\zeta = A u_{k,k} + \frac{\phi^2}{R} p \tag{5}$$

$$q_i = -\overline{k}\left(p_{,i} + \rho_{\mathcal{F}} \ddot{u}_i + \frac{\rho_0 + \phi \rho_{\mathcal{F}}}{\phi} \ddot{v}_i \right) \tag{6}$$

where $\rho_0 = \mu \varphi \rho_{\mathcal{F}}$, considering $\mu = 0.66$ [53].

For a domain $\mathbb{R}$, with the boundary $\mathbb{C}$, the initial and boundary conditions are

$$\dot{u}_i(\mathbf{x}, 0) = \ddot{u}_i(\mathbf{x}, 0), \tag{7}$$

$$u_i(\mathbf{x}, \tau) = \overline{u}_i(\mathbf{x}, \tau) \qquad \text{on } \mathbb{C}_1 \tag{8}$$

$$\lambda_i(\mathbf{x}, \tau) = \sigma_{ij}(\mathbf{x}, \tau)\, n_j = \overline{\lambda}_i(\mathbf{x}, \tau) \qquad \text{on } \mathbb{C}_2 \tag{9}$$

$$p(\mathbf{x}, \tau) = \overline{p}(\mathbf{x}, \tau) \qquad \text{on } \mathbb{C}_3 \tag{10}$$

$$L(\mathbf{x}, \tau) = \frac{\partial p(\mathbf{x}, \tau)}{\partial n} = \overline{L}(\mathbf{x}, \tau) \qquad \text{on } \mathbb{C}_4 \tag{11}$$

$$T(\mathbf{x}, 0) = T_0(\mathbf{x}) \tag{12}$$

$$T(\mathbf{x},\tau) = \widehat{T}(\mathbf{x},\tau), \qquad \text{on}\mathbb{C}_5 \tag{13}$$

$$q(\mathbf{x},\tau) = D_{x_1}\frac{\partial T}{\partial x_1}n_{x_1} + D_{x_2}\frac{\partial T}{\partial x_2}n_{x_2} = \widehat{q}(\mathbf{x},\tau), \quad \text{on}\mathbb{C}_6 \tag{14}$$

3. BEM for Anomalous Fractional Heat Diffusion Equation

The anomalous fractional anisotropic heat diffusion Equation (3) can be defined as the Caputo derivative as follows:

$$\frac{\partial_C^a T}{\partial \tau^a} = \frac{1}{\Gamma(1-a)}\int_0^\tau \frac{1}{(\tau-t)^a}\frac{\partial T(t)}{\partial t}dt, \quad 0 < a < 1 \tag{15}$$

The weighted residual equation is written as [55,56]

$$\int_{\mathbb{R}}\left[\frac{\partial_C^a T}{\partial t^a} - \left(D_{x_1}\frac{\partial^2 T}{\partial x_1^2} + D_{x_2}\frac{\partial^2 T}{\partial x_2^2}\right)\right]\chi d\Omega + \int_{\mathbb{C}_5}\left(T-\widehat{T}\right)\bar{\chi}d\Gamma + \int_{\mathbb{C}_6}(q-\widehat{q})\overline{\overline{\chi}}d\Gamma = 0 \tag{16}$$

The functions $\bar{\chi}$ and $\overline{\overline{\chi}}$ were selected as

$$\bar{\chi} = -\left(D_{x_1}\frac{\partial^2 \chi}{\partial x_1^2} + D_{x_2}\frac{\partial^2 \chi}{\partial x_2^2}\right) = \mathbb{Q} \tag{17}$$

and

$$\overline{\overline{\chi}} = \chi \tag{18}$$

Remembering that

$$D_{x_1}\frac{\partial^2 \chi}{\partial x_1^2} + D_{x_2}\frac{\partial^2 \chi}{\partial x_2^2} = -\delta(\mathbf{x}-\xi), \tag{19}$$

Based on the geometry of the considered problem, as shown in Figure 1 and Brebbia and Dominguez [55], the insertion of Equations (17)–(19) into Equation (16) produces the following boundary integral equation:

$$\begin{aligned} c(\xi)T(\xi,\tau) = &\int_{\mathbb{C}} q(\mathbf{x},\tau)w(\xi,\mathbf{x})\,d\Gamma(x) - \int_{\mathbb{C}} T(\mathbf{x},\tau)Q(\xi,\mathbf{x})\,d\Gamma(x) \\ &-\int_{\mathbb{R}} \frac{\partial_C^a T(\mathbf{x},\tau)}{\partial \tau^a}w(\xi,\mathbf{x})\,d\Omega(x) \end{aligned} \tag{20}$$

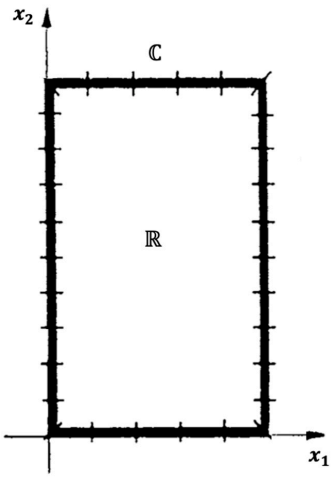

Figure 1. Geometry of the considered problem.

Based on Carrer et al. [57],

$$c(\xi) = 1,\ \xi \in \mathbb{R}$$

$$c(\xi) = \frac{1}{2\pi}\left[\tan^{-1}\left(\sqrt{\frac{D_{x_1}}{D_{x_2}}}\tan\theta_2\right) - \tan^{-1}\left(\sqrt{\frac{D_{x_1}}{D_{x_2}}}\tan\theta_1\right)\right],\ \xi \in \mathbb{C} \tag{21}$$

where angles θ_1 and θ_2 in Equation (21) are shown in Figure 2.

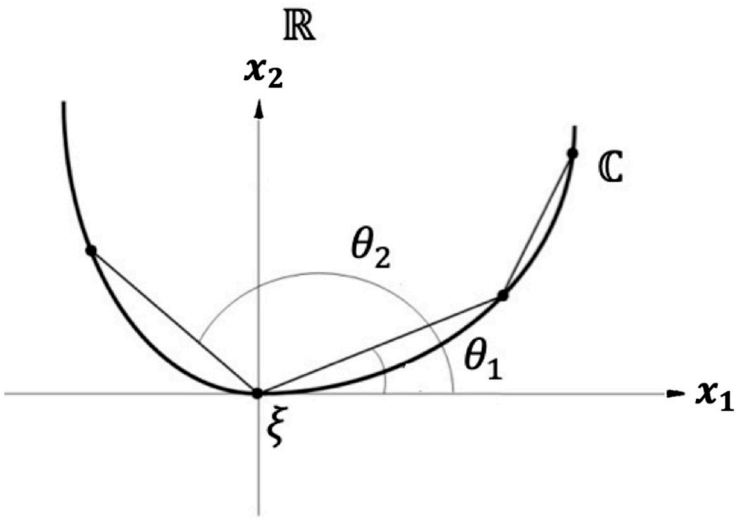

Figure 2. Angles configuration for estimation of $c(\xi)$.

The anisotropic fundamental solution is [58]

$$\chi = \chi(\xi, \mathbf{x}) = -\frac{1}{2\pi\sqrt{D_{x_1}D_{x_2}}}\ln\sqrt{(x_1-\xi_{x_1})^2 + \frac{D_{x_1}}{D_{x_2}}(x_2-\xi_{x_2})^2} \tag{22}$$

For isotropic material, $D_{x_1} = D_{x_2} = D$ and Equations (21) and (22) become

$$\chi(\xi, \mathbf{x}) = -\frac{1}{2\pi D}\ln\sqrt{(x_1-\xi_{x_1})^2 + (x_2-\xi_{x_2})^2} = -\frac{1}{2\pi D}\ln r \tag{23}$$

and

$$c(\xi) = \frac{\theta_2 - \theta_1}{2\pi} \tag{24}$$

For the computing integral in Equation (15), we consider $\tau_{n+1} = (n+1)\Delta\tau, 0 \le \tau \le \tau_{n+1}$, and $T_k = T(\mathbf{x}, \tau_k) = T_k(\mathbf{x})$ to obtain [59]

$$T = \frac{(\tau_{k+1} - t)}{\Delta\tau}T_k + \frac{(t-\tau_k)}{\Delta\tau}T_{k+1} \tag{25}$$

and consequently,

$$\frac{\partial T}{\partial t} = \frac{T_{k+1} - T_k}{\Delta\tau} \tag{26}$$

Finally, the Caputo derivative is

$$\begin{aligned}\left.\frac{\partial_C^a T}{\partial\tau^a}\right|_{t=t_{n+1}} = \frac{1}{\Gamma(1-\alpha)}\Bigg[&\int_0^{\tau_1}\frac{1}{(\tau_1-t)^\alpha}\frac{(u_1-u_0)}{\Delta\tau}dt + \int_{t_1}^{\tau_2}\frac{1}{(\tau_2-t)^\alpha}\frac{(u_2-u_1)}{\Delta\tau}dt + \ldots + \\ &\int_{t_k}^{\tau_{k+1}}\frac{1}{(\tau_{k+1}-t)^\alpha}\frac{(u_{k+1}-u_k)}{\Delta\tau}dt + \ldots + \int_{t_n}^{\tau_{n+1}}\frac{1}{(\tau_{n+1}-t)^\alpha}\frac{(u_{n+1}-u_n)}{\Delta\tau}dt\Bigg]\end{aligned} \tag{27}$$

Now, Equation (27) yields

$$\left.\frac{\partial_C^a T}{\partial \tau^a}\right|_{t=t_{n+1}} = \frac{1}{\Gamma(2-a)\Delta\tau^a}\left[T_{n+1} - T_n + \sum_{j=0}^{n-1}\left(\frac{1}{(n+1-j)^{a-1}} - \frac{1}{(n-j)^{a-1}}\right)\left(T_{j+1} - T_j\right)\right] \tag{28}$$

which can be expressed as

$$\left.\frac{\partial_C^\alpha T}{\partial \tau^\alpha}\right|_{\tau=\tau_{n+1}} = \frac{1}{\Gamma(2-a)\Delta\tau^a}\left[T_{n+1} - T_n + \sum_{j=0}^{n-1} B_{(n+1),(j+1)}\left(T_{j+1} - T_j\right)\right],\ n \geq 1 \tag{29}$$

where

$$B_{(n+1),(j+1)} = \frac{1}{(n+1-j)^{a-1}} - \frac{1}{(n-j)^{a-1}} \tag{30}$$

For $n = 0$, Equation (28) can be written as

$$\left.\frac{\partial_C^\alpha T}{\partial \tau^a}\right|_{t=t_1} = \frac{1}{\Gamma(2-a)\Delta\tau^a}[T_1 - T_0] \tag{31}$$

Substituting (28) into (20), we obtain

$$\begin{aligned} c(\xi)T_{n+1}(\xi) = &\int_{\mathbb{C}} q_{n+1}(\mathbf{x})\chi(\xi,\mathbf{x})d\mathbb{C}(\mathbf{x}) - \int_{\mathbb{C}} T_{n+1}(\mathbf{x})Q(\xi,\mathbf{x})d\mathbb{C}(\mathbf{x}) - \\ &\frac{1}{\Gamma(2-a)\Delta\tau^\alpha}\int_{\mathbb{R}}\left[T_{n+1}(\mathbf{x}) - T_n(\mathbf{x}) + \sum_{j=0}^{n-1} B_{(n+1),(j+1)}\left(T_{j+1}(\mathbf{x}) - T_j(\mathbf{x})\right)\right]\chi(\xi,\mathbf{x})d\mathbb{R}(\mathbf{x}) \end{aligned} \tag{32}$$

Equation (32) requires that the boundary be discretized into linear elements. Assume that T and q vary linearly along each element in the border discretization. To compute the domain integral, the entire domain must be divided into linear triangle cells. Assume that T varies linearly across the cells in the domain discretization. Thus, the matrix form of Equation (32) is as follows:

$$\begin{aligned} \begin{bmatrix} \boldsymbol{G}^{bb} & 0 \\ \boldsymbol{G}^{db} & \boldsymbol{I} \end{bmatrix}\begin{Bmatrix} \boldsymbol{T}^b_{n+1} \\ \boldsymbol{T}^d_{n+1} \end{Bmatrix} = &\begin{bmatrix} \boldsymbol{H}^{bb} \\ \boldsymbol{H}^{db} \end{bmatrix}\left\{\boldsymbol{q}^b_{n+1}\right\} - \begin{bmatrix} \boldsymbol{N}^{bb} & \boldsymbol{N}^{bd} \\ \boldsymbol{N}^{db} & \boldsymbol{N}^{dd} \end{bmatrix}\begin{Bmatrix} \boldsymbol{T}^b_{n+1} - \boldsymbol{T}^b_n \\ \boldsymbol{T}^d_{n+1} - \boldsymbol{T}^d_n \end{Bmatrix} \\ &- \begin{bmatrix} \boldsymbol{N}^{bb} & \boldsymbol{N}^{bd} \\ \boldsymbol{N}^{db} & \boldsymbol{N}^{dd} \end{bmatrix}\sum_{j=0}^{n-1} B_{(n+1),(j+1)}\begin{Bmatrix} \boldsymbol{T}^b_{j+1} - \boldsymbol{T}^b_j \\ \boldsymbol{T}^d_{j+1} - \boldsymbol{T}^d_j \end{Bmatrix} \end{aligned} \tag{33}$$

which can be expressed as [59]

$$\begin{aligned} \begin{bmatrix} \left(\boldsymbol{G}^{bb} + \boldsymbol{N}^{bb}\right) & \boldsymbol{N}^{bd} \\ \left(\boldsymbol{G}^{db} + \boldsymbol{N}^{db}\right) & \left(\boldsymbol{I} + \boldsymbol{N}^{dd}\right) \end{bmatrix}\begin{Bmatrix} \boldsymbol{T}^b_{n+1} \\ \boldsymbol{T}^d_{n+1} \end{Bmatrix} = &\begin{bmatrix} \boldsymbol{H}^{bb} \\ \boldsymbol{H}^{db} \end{bmatrix}\left\{\ \boldsymbol{q}^b_{n+1}\ \right\} + \begin{bmatrix} \boldsymbol{N}^{bb} & \boldsymbol{N}^{bd} \\ \boldsymbol{N}^{db} & \boldsymbol{N}^{dd} \end{bmatrix}\begin{Bmatrix} \boldsymbol{T}^b_n \\ \boldsymbol{T}^d_n \end{Bmatrix} \\ &- \begin{bmatrix} \boldsymbol{N}^{bb} & \boldsymbol{N}^{bd} \\ \boldsymbol{N}^{db} & \boldsymbol{N}^{dd} \end{bmatrix}\sum_{j=0}^{n-1} B_{(n+1),(j+1)}\begin{Bmatrix} \boldsymbol{T}^b_{j+1} - \boldsymbol{T}^b_j \\ \boldsymbol{T}^d_{j+1} - \boldsymbol{T}^d_j \end{Bmatrix} \end{aligned} \tag{34}$$

where source and field locations are indicated by double superscripts, the first of which shows the location of the former and the second the position of the latter, and superscripts b and d stand for the boundary and domain variables, respectively.

4. BEM for Displacement of Cement-Based Materials

Using the weighted residual approach on Equations (1) and (2), we get

$$\int_{\mathbb{R}}\left(\sigma_{ij,j} + U_i\right)u_i^*\, d\mathbb{R} = 0 \tag{35}$$

$$\int_{\mathbb{R}}\left(q_{,i} + \dot{\zeta}_i - \overline{\mathbb{C}_i}\right)p_i^*\, d\mathbb{R} = 0 \tag{36}$$

where u_i^* and p_i^* are weighting functions, $U_i = -\left(\rho\ddot{u}_i + \phi\rho_{\mathcal{F}}\ddot{v}_i\right)$

By integrating Equations (35) and (36), we get

$$-\int_{\mathbb{R}} \sigma_{ij}\, u^*_{i,j}\, d\mathbb{R} + \int_{\mathbb{R}} U_i\, u^*_i\, d\mathbb{R} = -\int_{\mathbb{C}_2} \lambda_i\, u^*_i\, d\mathbb{C} \tag{37}$$

$$-\int_{R} q\, \mathrm{p}^*_{i,i}\, dR + \int_{R} \dot{\zeta}_i\, \mathrm{p}^*_i\, dR - \int_{R} \overline{\mathbb{C}_i}\, \mathrm{p}^*_i\, dR = -\int_{\mathbb{C}_4} L_i\, \mathrm{p}^*_i\, dS \tag{38}$$

Huang and Liang [60] suggested the following boundary integral equation:

$$\begin{array}{l} -\int_{\mathbb{R}} \sigma_{ij,j}\, u^*_i\, d\mathbb{R} \quad + \int_{\mathbb{R}} U_i\, u^*_i\, d\mathbb{R} - \int_{\mathbb{R}} q\, \mathrm{p}^*_{i,i}\, d\mathbb{R} + \int_{\mathbb{R}} \dot{\zeta}_i\, \mathrm{p}^*_i\, d\mathbb{R} - \int_{\mathbb{R}} \overline{\mathbb{C}_i}\, \mathrm{p}^*_i\, d\mathbb{R} \\ \quad = \int_{\mathbb{C}_2} \left(\lambda_i - \overline{\lambda}_i\right) u^*_i\, d\mathbb{C} + \int_{\mathbb{C}_1} \left(\overline{u}_i - u_i\right) \lambda^*_i\, d\mathbb{C} + \int_{\mathbb{C}_4} \left(L_i - \overline{L}_i\right)\, \mathrm{p}^*_i\, d\mathbb{C} + \int_{\mathbb{C}_3} \left(\overline{\mathrm{p}}_i - \mathrm{p}_i\right) L^*_i\, d\mathbb{C} \end{array} \tag{39}$$

By integrating (39), we get

$$\begin{array}{l} -\int_{\mathbb{R}} \sigma_{ij}\, \varepsilon^*_{ij}\, d\mathbb{R} \quad + \int_{\mathbb{R}} U_i\, u^*_i\, d\mathbb{R} - \int_{\mathbb{R}} q\, \mathrm{p}^*_{i,i}\, d\mathbb{R} + \int_{\mathbb{R}} \dot{\zeta}_i\, \mathrm{p}^*_i\, d\mathbb{R} - \int_{\mathbb{R}} \overline{\mathbb{C}_i}\, \mathrm{p}^*_i\, d\mathbb{R} \\ \quad = -\int_{\mathbb{C}_2} \overline{\lambda}_i\, u^*_i\, d\mathbb{C} - \int_{\mathbb{C}_1} \lambda_i\, u^*_i\, d\mathbb{C} + \int_{\mathbb{C}_1} \left(\overline{u}_i - u_i\right) \lambda^*_i\, d\mathbb{C} - \int_{\mathbb{C}_4} \overline{L}_i\, \mathrm{p}^*_i\, d\mathbb{C} - \int_{\mathbb{C}_4} L_i\, \mathrm{p}^*_i\, d\mathbb{C} \\ \quad + \int_{\mathbb{C}_3} \left(\overline{\mathrm{p}}_i - \mathrm{p}_i\right) L^*_i\, d\mathbb{C} \end{array} \tag{40}$$

Eringen [61] defines elastic stress as

$$\sigma_{ij} = \mathbb{a}_{ijkl}\, \varepsilon_{kl}, \text{ where } \mathbb{a}_{ijkl} = \mathbb{a}_{klij} \tag{41}$$

Consequently, Equation (40) can be written as

$$\begin{array}{l} -\int_{\mathbb{R}} \sigma^*_{ij}\, \varepsilon_{ij}\, d\mathbb{R} \quad + \int_{\mathbb{R}} U_i\, u^*_i\, d\mathbb{R} - \int_{\mathbb{R}} q\, \mathrm{p}^*_{i,i}\, d\mathbb{R} + \int_{\mathbb{R}} \dot{\zeta}_i\, \mathrm{p}^*_i\, d\mathbb{R} - \int_{\mathbb{R}} \overline{\mathbb{C}_i}\, \mathrm{p}^*_i\, d\mathbb{R} \\ \quad = -\int_{\mathbb{C}_2} \overline{\lambda}_i\, u^*_i\, d\mathbb{C} - \int_{\mathbb{C}_1} \lambda_i\, u^*_i\, d\mathbb{C} + \int_{\mathbb{C}_1} \left(\overline{u}_i - u_i\right) \lambda^*_i\, d\mathbb{C} - \int_{\mathbb{C}_4} \overline{L}_i\, \mathrm{p}^*_i\, d\mathbb{C} - \int_{\mathbb{C}_4} L_i\, \mathrm{p}^*_i\, d\mathbb{C} \\ \quad + \int_{\mathbb{C}_3} \left(\overline{\mathrm{p}}_i - \mathrm{p}_i\right) L^*_i\, d\mathbb{C} \end{array} \tag{42}$$

By integrating (42), we get

$$\int_{\mathbb{R}} \sigma^*_{ij,j}\, u_i\, d\mathbb{R} = -\int_{\mathbb{C}} u^*_i\, \lambda_i\, d\mathbb{C} - \int_{\mathbb{C}} \mathrm{p}^*_i\, L_i\, d\mathbb{C} + \int_{\mathbb{C}} \lambda^*_i\, u_i\, d\mathbb{C} + \int_{\mathbb{C}} L^*_i\, \mathrm{p}_i\, d\mathbb{C} \tag{43}$$

Now, the weighting functions and the fundamental solution for $U_i = \Delta^n$ are [62]

$$\sigma^*_{lj,j} + \Delta^n e_l = 0 \tag{44}$$

$$u^*_i = u^*_{li}\, e_l, \;\; \lambda^*_i = \lambda^*_{li}\, e_l, \; p^*_i = p^*_{li}\, e_l, L^*_i = L^*_{li}\, e_l \tag{45}$$

Also, the weighting functions and the fundamental solution for $U_i = 0$ are [62]

$$\sigma^{**}_{ij,j} = 0 \tag{46}$$

$$u^*_i = u^{**}_{li}\, e_l, \; p^*_i = p^{**}_{li}\, e_l, \lambda^*_i = \lambda^{**}_{li}\, e_l, L^*_i = L^{**}_{li}\, e_l \tag{47}$$

Now, from Equation (43), we have

$$\mathrm{g}^n_{li} u^n_i = -\int_S \lambda^*_{li}\, u_i\, dS - \int_S \mathrm{L}^*_{li}\, p_i\, dS + \int_S u^*_{li}\, \lambda_i\; dS + \int_S p^*_{li}\, \mathrm{L}_i\; dS \tag{48}$$

$$0 = -\int_S \lambda^{**}_{li}\, u_i\, dS - \int_S \mathrm{L}^{**}_{li}\, p_i\, dS + \int_S u^{**}_{li}\, \lambda_i\; dS + \int_S p^{**}_{li}\, \mathrm{L}_i\; dS \tag{49}$$

which can be expressed as

$$\mathrm{g}^n \mathbb{F}^n = -\int_S \mathbb{E}^* \mathbb{F}\, dS + \int_S \mathbb{F}^* \mathbb{E}\, dS + \int_S \mathbb{a}^*\, \mathrm{p}\; dS + \int_S \mathbb{b}^*\, \frac{\partial \mathrm{p}}{\partial n}\; dS \tag{50}$$

in which

$$\mathrm{g}^n = \begin{bmatrix} \mathrm{g}_{11} & \mathrm{g}_{12} \\ \mathrm{g}_{21} & \mathrm{g}_{22} \end{bmatrix},\ \mathbb{F}^* = \begin{bmatrix} u_{11}^* & u_{12}^* \\ u_{21}^* & u_{22}^* \end{bmatrix},\ \mathbb{E}^* = \begin{bmatrix} \lambda_{11}^* & \lambda_{12}^* \\ \lambda_{21}^* & \lambda_{22}^* \end{bmatrix}, \mathbb{F} = \begin{bmatrix} u_1 \\ u_2 \end{bmatrix},$$

$$\mathbb{E} = \begin{bmatrix} \lambda_1 \\ \lambda_2 \end{bmatrix},\ \mathbb{a}^* = \begin{bmatrix} \mathbb{a}_1^* \\ \mathbb{a}_2^* \end{bmatrix},\ \mathbb{b}^* = \begin{bmatrix} \mathbb{b}_1^* \\ \mathbb{b}_2^* \end{bmatrix} \tag{51}$$

We now present the following equations:

$$\mathbb{F} = \Psi\ \mathbb{F}^j, \mathbb{E} = \Psi\ \mathbb{E}^j,\ p = \Psi_0\ p^j,\ \frac{\partial p}{\partial n} = \Psi_0 \left(\frac{\partial p}{\partial n}\right)^j \tag{52}$$

The discretization of the boundary allows us to use (52) into (50) to obtain

$$\mathrm{g}^n \mathbb{F}^n = \sum_{j=1}^{N_e} \left[-\int_{\Gamma_j} \mathbb{E}^* \Psi\ d\Gamma \right] \mathbb{F}^j + \sum_{j=1}^{N_e} \left[\int_{\Gamma_j} \mathbb{F}^* \Psi\ d\Gamma \right] \mathbb{E}^j + \sum_{j=1}^{N_e} \left[\int_{\Gamma_j} \mathbb{a}^* \Psi_0\ d\Gamma \right] p^j + \sum_{j=1}^{N_e} \left[\int_{\Gamma_j} \mathbb{b}^* \Psi_0\ d\Gamma \right] \left(\frac{\partial p}{\partial n}\right)^j \tag{53}$$

It is possible to state as

$$\mathrm{g}^i \mathbb{F}^i = -\sum_{j=1}^{N_e} \hat{\mathbb{G}}^{ij} \mathbb{F}^j + \sum_{j=1}^{N_e} \hat{\mathbb{H}}^{ij} \mathbb{E}^j + \sum_{j=1}^{N_e} \hat{\mathbb{a}}^{ij} p^j + \sum_{j=1}^{N_e} \hat{\mathbb{b}}^{ij} \left(\frac{\partial p}{\partial n}\right)^j \tag{54}$$

By employing the following formula:

$$\mathbb{G}^{ij} = \begin{cases} \hat{\mathbb{G}}^{ij} & if\ \ i \neq j \\ \hat{\mathbb{G}}^{ij} + \mathrm{g}^i & if\ \ i = j \end{cases} \tag{55}$$

Equation (54) can be represented as

$$\sum_{j=1}^{N_e} \mathbb{G}^{ij} \mathbb{F}^j = \sum_{j=1}^{N_e} \hat{\mathbb{H}}^{ij} \mathbb{E}^j + \sum_{j=1}^{N_e} \hat{\mathbb{a}}^{ij} p^j + \sum_{j=1}^{N_e} \hat{\mathbb{b}}^{ij} \left(\frac{\partial p}{\partial n}\right)^j \tag{56}$$

This can be stated as

$$\mathbb{G}\mathbb{U} = \mathbb{H}\mathbb{T} + \mathbb{a}\mathbb{i} + \mathbb{b}\mathbb{j} \tag{57}$$

where $\mathbb{U}$ symbolizes displacements and $\mathbb{T}$ represents tractions.

Equation (57) can now be expressed as

$$\mathbb{a}\mathbb{X} = \mathbb{b} \tag{58}$$

In Matlab (R2018a), a modified hybrid explicit group (MHEG) of the Salama et al. [63] method has been efficiently applied for solving Equations (34) and (58).

5. Thermal Stress Intensity Factor of Cement-Based Materials

Based on crack propagation of mode-I fracture in concrete [64] as an example for considered cement-based materials and using [65,66], the mathematical relationship between the cohesive stress σ_c and crack opening displacement u, which is used to describe the softening behavior of concrete, is as follows:

$$\sigma_c(x) = s_t - (s_t - \sigma_b)\frac{u}{u_s},\ 0 \leq u \leq u_s \tag{59}$$

$$\sigma_c(x) = \sigma_b \frac{u_0 - u}{u_0 - u_s},\ u_s \leq u \leq u_0 \tag{60}$$

$$\sigma_c(x) = 0,\ \ u \geq u_0 \tag{61}$$

The thermal stress intensity factor (SIF) at the crack tip in a three-point beam caused by cohesive force for the considered problem is

$$K_I = \frac{\int_{a_0}^{a} 2\sigma_c(x) G\left(\frac{x}{\ell}, \frac{\ell}{d}\right)}{\sqrt{\pi \ell} dx} \tag{62}$$

where

$$G(x/\ell, \ell/d) = \overline{F} - \overline{\overline{F}} + \overline{G} \times \overline{\overline{G}}$$

$$\overline{F} = \frac{3.52(1 - x/\ell)}{(1 - \ell/d)^{3/2}}, \ \overline{\overline{F}} = \frac{4.35 - 5.28(x/\ell)}{(1 - \ell/d)^{1/2}}, \ \overline{G} = \left[\frac{1.3 - 0.3(x/\ell)^{3/2}}{\sqrt{1 - (x/\ell)^2}} + 0.83 - 1.76(x/\ell)\right]$$

$$\overline{\overline{G}} = [1 - (1 - x/\ell)(\ell/d)]$$

6. Numerical Results and Discussion

To demonstrate the numerical results produced utilizing the proposed methodology, we considered anisotropic asphalt concrete properties, as given in reference [23], as an example for considered cement-based materials at $\Delta\tau = 0.0001$.

Figure 3 depicts the anomalous temperature T distribution in cement-based materials, where the anomalous temperature T begins at zero and then oscillates as the distance x_1 increases, reaching a maximum value for $a = 0.50$, which is greater than the T values at fractional-order parameter value $a = 1.0$, which corresponds to the classical temperature model. It is also obvious that oscillation increases with small fractional-order parameters and reduces with large fractional-order parameters. This figure also illustrates that the fractional parameter has a considerable impact on temperature T in cement-based materials.

Figure 4 shows the anomalous heat flux q distribution in the cement-based materials, where the magnitude range of the anomalous heat flux q expands with the fractional-order parameter for small and medium values, reaching a maximum value at $a = 0.75$, within the high-value range of the anomalous displacement model, while q values during the high values of anomalous displacement model are higher than the q values at fractional-order parameter value $a = 1.00$, which corresponds to the classical displacement model. The anomalous q begins at zero, then oscillates as the distance x_1 increases. It is also clear that the oscillation grows as the fractional-order parameter's value increases. This figure also shows that the fractional parameter significantly impacts the anomalous q in cement-based materials.

Figure 5 shows the anomalous fluid flux q_a distribution in the cement-based materials, where the magnitude range of the anomalous fluid flux q_a, expands with the fractional-order parameter for small and medium values, reaching a maximum value at $a = 0.75$, within the high-value range of the anomalous displacement model, while q_a values during the high values of the anomalous displacement model are higher than the q_a values at fractional-order parameter value $a = 1.00$, which corresponds to the classical displacement model. The anomalous q_a begins at zero and then oscillates as the distance x_1 increases. It is also clear that the oscillation grows as the fractional-order parameter's value increases. This figure also shows that the fractional parameter significantly impacts the anomalous q_a in cement-based materials.

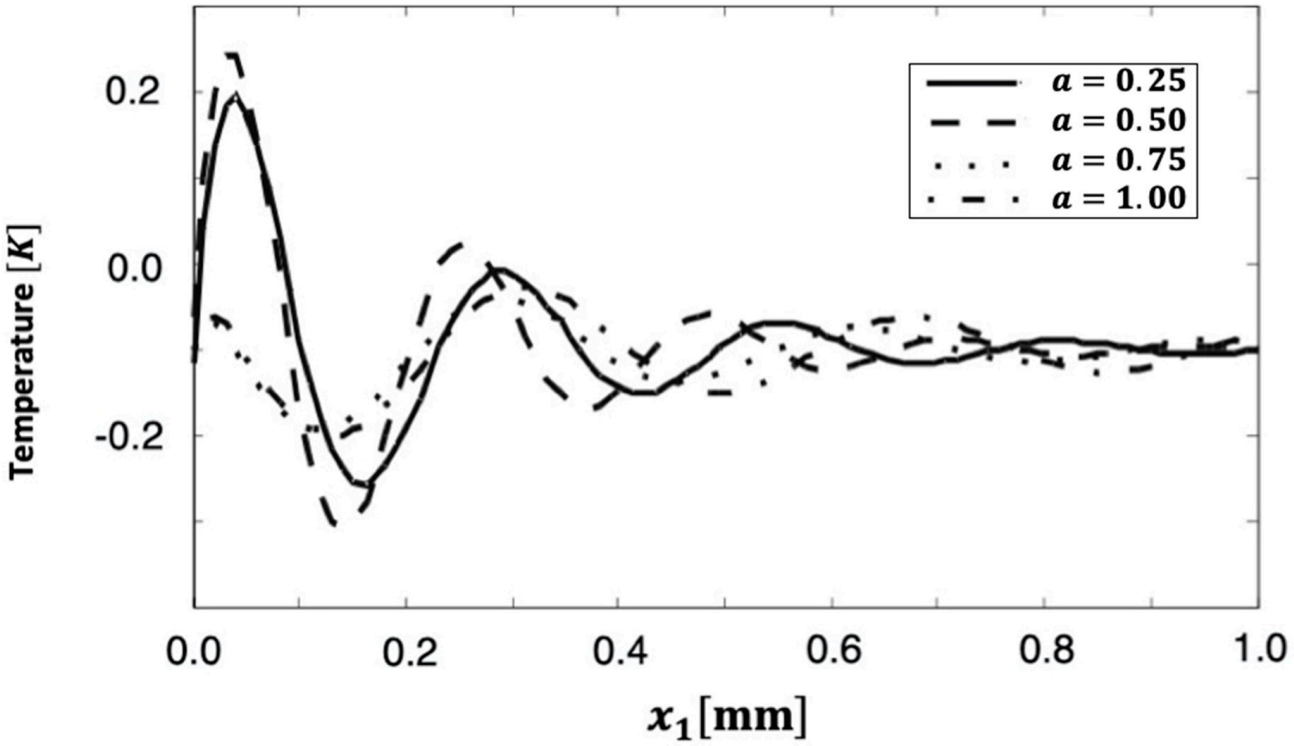

Figure 3. Anomalous temperature distribution along x_1 axis for various fractional parameter values ($a = 0.25,\ 0.50,\ 0.75$ and 1.00).

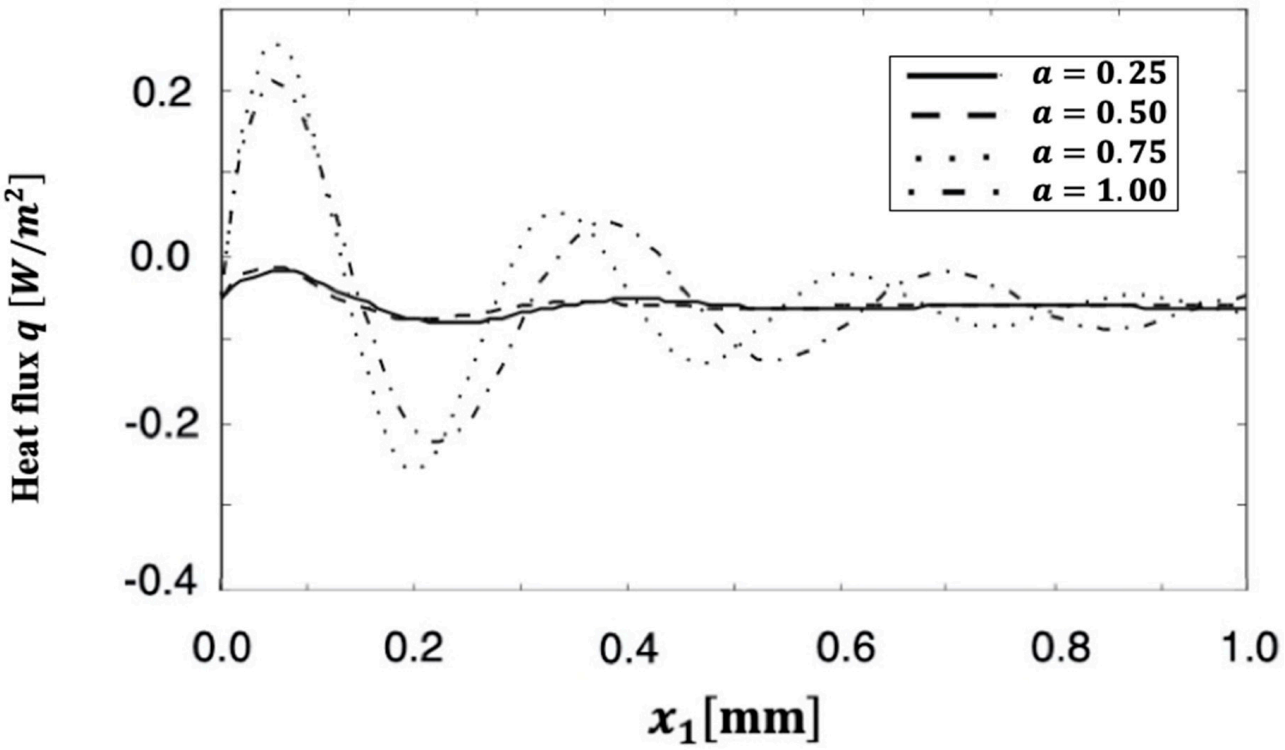

Figure 4. Anomalous heat flux q distribution along x_1 axis for various fractional parameter values ($a = 0.25,\ 0.50,\ 0.75$ and 1.00).

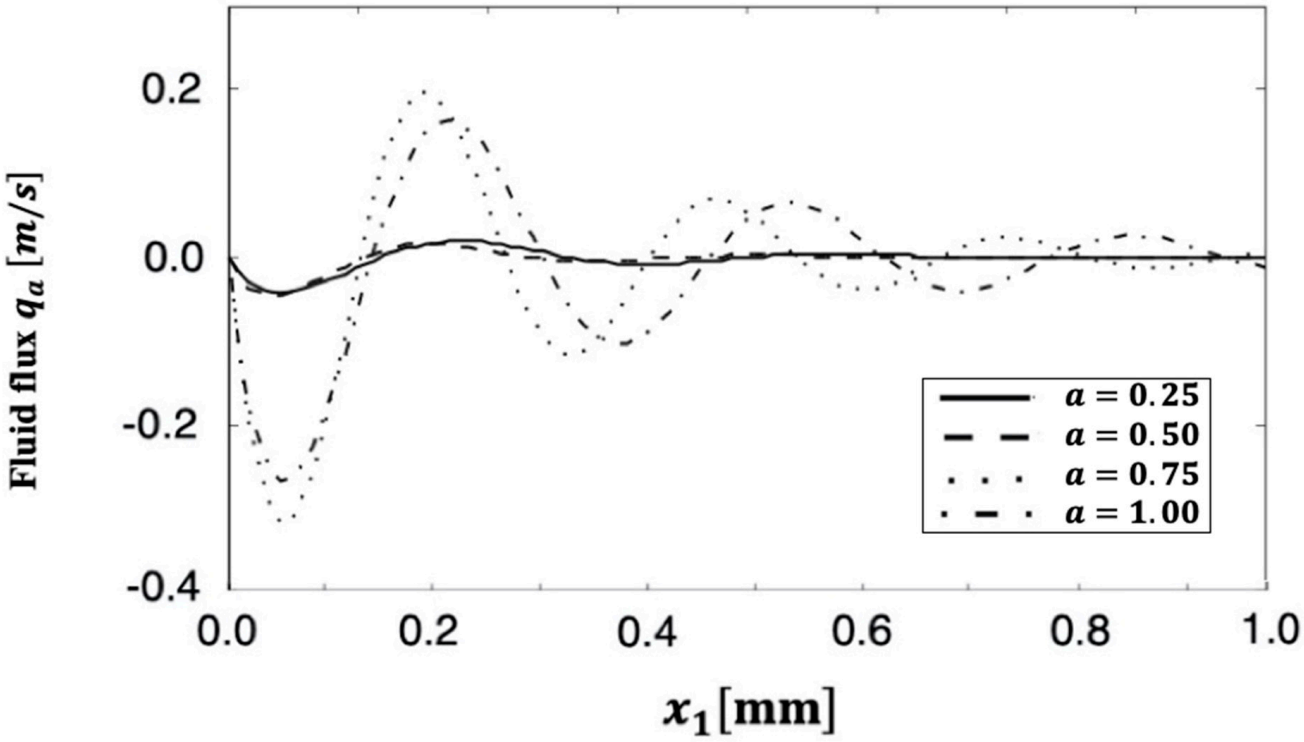

Figure 5. Anomalous fluid flux q_a distribution along x_1 axis for various fractional parameter values ($a = 0.25,\ 0.50,\ 0.75$ and 1.00).

Figures 5–7 show the anomalous thermal stress σ_{11}, σ_{12}, and σ_{22} distributions along x_1 axis for various fractional parameter values ($a = 0.25,\ 0.50,\ 0.75,$ and 1.00) in cement-based materials.

Figure 6 demonstrates that the magnitude range of the anomalous thermal stress σ_{11} increases with the fractional-order parameter until the maximum value at $a = 1.00$, which corresponds to the classical thermal stress model. This figure also shows that the thermal stress σ_{11} begins at zero and oscillates as the distance x_1 grows. It is also obvious that the oscillation increases as the value of the fractional-order parameter increases. The figure shows how the fractional-order parameter affects the anomalous thermal stress σ_{11} of cement-based materials.

Figure 7 indicates that the magnitude range of the anomalous thermal stress, σ_{12}, expands with the fractional-order parameter, reaching a maximum value at $a = 1.00$, which corresponds to the classical thermal stress model. The thermal stress σ_{12} starts at zero and oscillates as the distance x_1 increases. It is also clear that the oscillation grows as the fractional-order parameter's value increases. This graphic illustrates how the fractional parameter has a considerable impact on the anomalous σ_{12} of cement-based materials.

Figure 8 shows a distinct status for the anomalous thermal stress σ_{22} in the cement-based materials, where the magnitude range of the anomalous thermal stress, σ_{22}, expands with the fractional-order parameter for small and medium values, reaching a maximum value at $a = 0.75$, within the high-value range of the anomalous thermal stress model, while σ_{22} values during the high values of the anomalous thermal stress model are higher than the σ_{22} values at fractional-order parameter value $a = 1.00$, which corresponds to the classical thermal stress model. The anomalous σ_{22} begins at zero, then oscillates as the distance x_1 increases. It is also clear that the oscillation grows as the fractional-order parameter's value increases. This figure also shows that the fractional parameter significantly impacts the anomalous σ_{22} in cement-based materials.

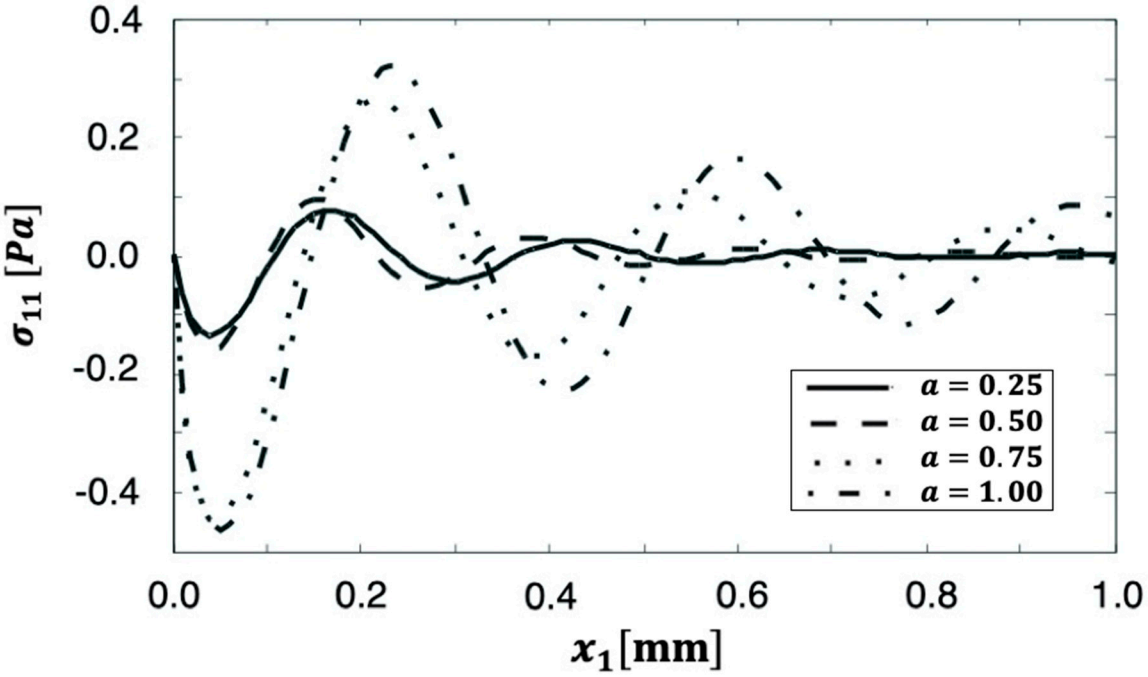

Figure 6. Anomalous thermal stress σ_{11} distribution along x_1 axis for various fractional parameter values ($a = 0.25,\ 0.50,\ 0.75$ and 1.00).

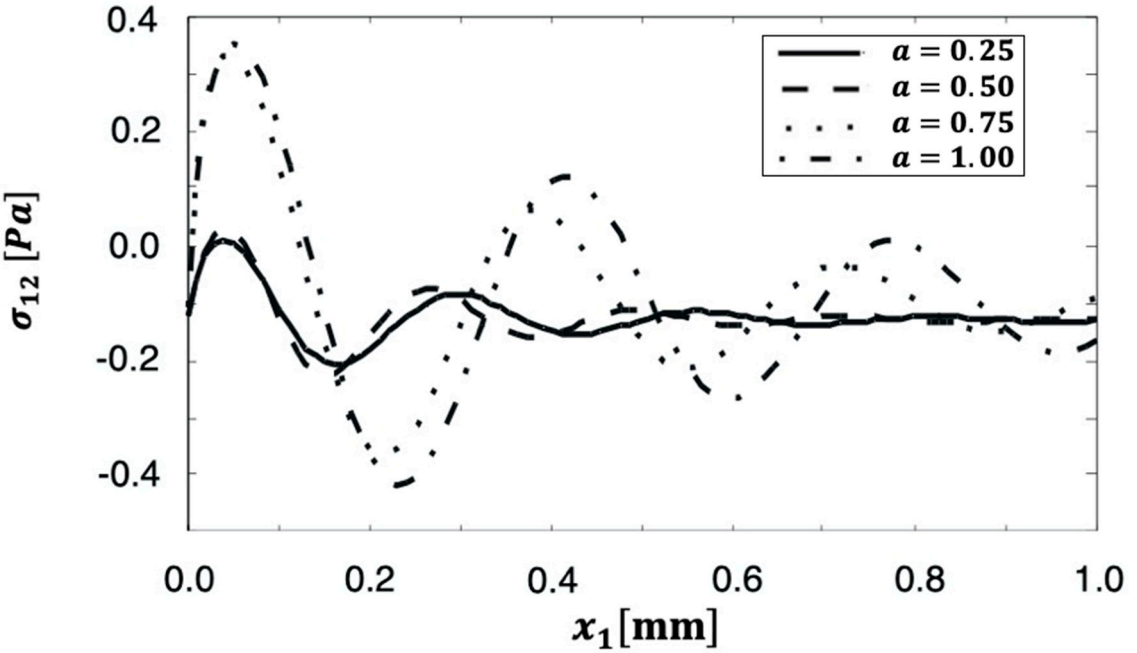

Figure 7. Anomalous thermal stress σ_{12} distribution along x_1 axis for various fractional parameter values ($a = 0.25,\ 0.50,\ 0.75$ and 1.00).

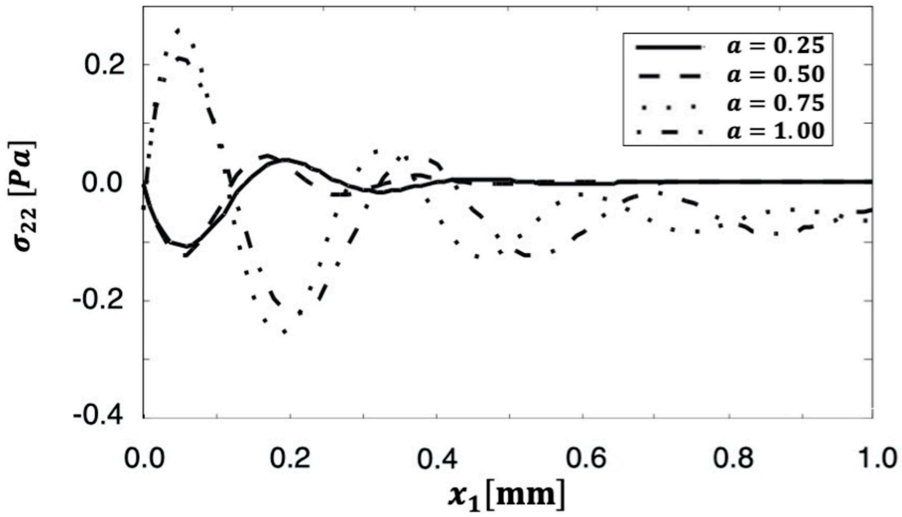

Figure 8. Anomalous thermal stress σ_{22} distribution along x_1 axis for various fractional parameter values $(a = 0.25,\ 0.50,\ 0.75$ and $1.00)$.

There are no findings available for the problem being investigated. As a result, various publications can be viewed as special cases within our BEM general problem. For comparison reasons with the exceptional circumstances of other methodologies treated by other authors, we examined the conditions of these investigations [67–70] and compared their findings to those of the current study. In the special instance under examination, the findings are displayed in Figures 9–11 to show the anomalous thermal stresses σ_{11}, σ_{12}, and σ_{22} distributions along x_1 axis for various approaches. Comparison with previously published results [67–70], which are also provided as a particular instance of our results concerning anomalous thermal stresses in cement-based materials, where we compared our BEM results to those of the finite element method (FEM) results of Cifuentes et al. [67], which match the experimental results of RILEM [68] and the combination model FDM-FEM of Do [69], which matches ABAQUS finite element model of Lin and Chen [70]. These findings show that the existing BEM is very consistent with FEM [67] and FDM-FEM [69], demonstrating the reliability and accuracy of our proposed technique. The computational results for the topic at hand were achieved.

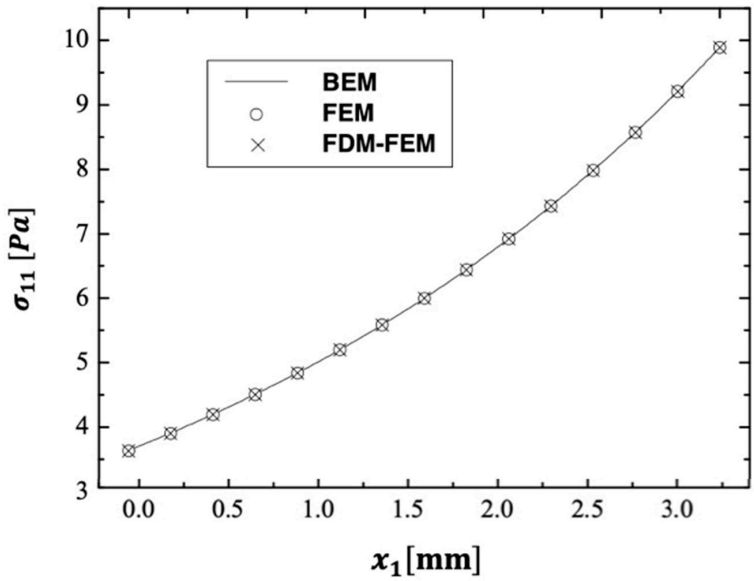

Figure 9. Special-case anomalous thermal stress σ_{11} distribution along x_1 axis for various methods.

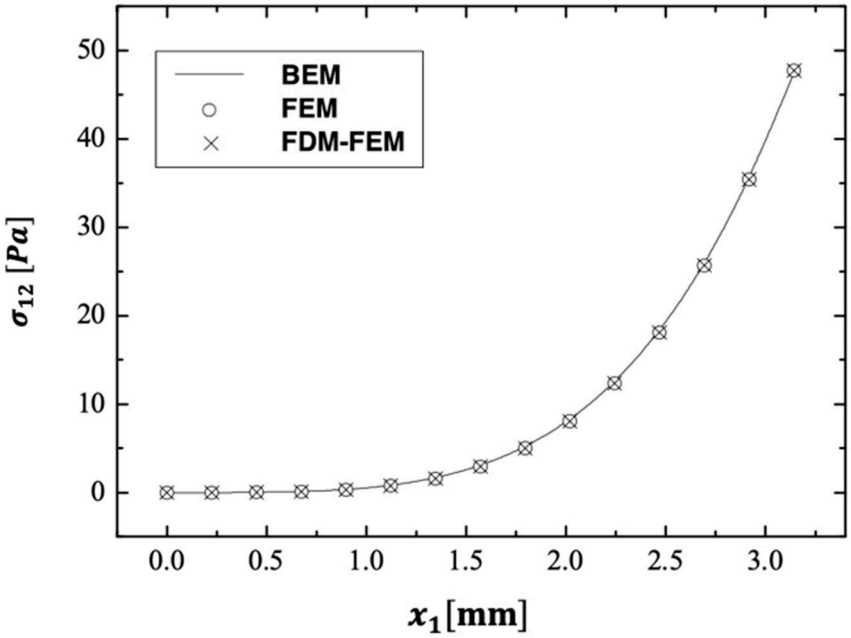

Figure 10. Special-case anomalous thermal stress σ_{12} distribution along x_1 axis for various methods.

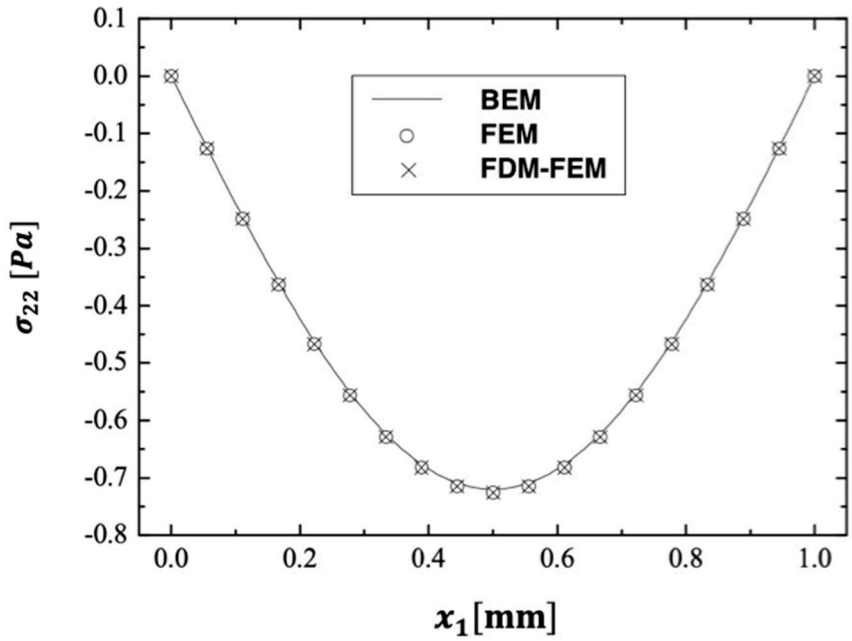

Figure 11. Special-case anomalous thermal stress σ_{22} distribution along x_1 axis for various methods.

Table 1 shows the CPU timings and iteration counts for the modified hybrid explicit group (MHEG) of Salama et al. [63], the modified symmetric successive overrelaxation (MSSOR) of Darvishi and Hessari [71], and the modified accelerated successive overrelaxation (MAOR) of Hadjidirnos et al. [72] iterative approaches at every discretization level, with equation numbers included in brackets. This table demonstrates that the MHEG methodology performs better than the MSSOR and MAOR strategies.

Table 1. Processor timings and execution counts for MSSOR, MAOR, and MHEG.

Discretization Level	Preconditioning Level	MSSOR		MAOR		MHEG	
		Processor Timings	Execution Counts	Processor Timings	Execution Counts	Processor Timings	Execution Counts
1 (28)	0	0.07	7	0.09	7	0.06	7
2 (56)	0	0.19	9	0.24	9	0.17	8
	1	0.16	7	0.2	7	0.12	7
3 (112)	0	0.48	11	0.64	12	0.42	10
	1	0.44	9	0.56	10	0.34	7
	2	0.38	7	0.5	8	0.3	5
4 (224)	0	2.42	14	2.52	18	1.88	12
	1	1.86	12	2.1	16	1.58	8
	2	1.58	8	1.84	12	1.42	6
	3	1.44	6	1.58	8	1.38	4
5 (448)	0	10.86	16	13.01	20	8.78	14
	1	9.2	14	11.12	18	7.79	10
	2	9.28	12	10.28	16	7.08	8
	3	8.26	10	9.42	12	6.69	6
	4	8.1	6	8.98	8	6.12	4
6 (896)	0	42.3	22	48.6	24	36	16
	1	38.6	20	46.7	22	34.2	14
	2	37.5	18	44.4	20	32.5	12
	3	35.4	14	40.7	16	30.7	10
	4	28.5	12	30.6	14	26.6	8
	5	24.8	10	28.8	12	20.8	4

Table 2 compares the computational needs for modeling anomalous thermal stress effects on cement-based materials utilizing current BEM, FEM [67], and FDM-FEM [69]. This table illustrates the effectiveness of the proposed BEM technique.

Table 2. An analysis of the computational power required to predict anomalous thermal stress effects on cement-based materials.

	BEM	FEM [64]	FDM-FEM [66]
Number of nodes	56	60,000	58,000
Number of elements	20	11,000	10,000
CPU time [min]	2	200	220
Memory [Mbyte]	1	160	150
Disk space [Mbyte]	0	270	290
Accuracy of results [%]	1.0	2.6	2.2

Based on a comparison of the calculated and experimental results of RILEM [68], mesh convergence research is performed utilizing $N_e = 10,\ 50$ and 90 linear elements for thermal stress intensity factor (SIF) distribution along the x_1 axis, as shown in Figure 12. This figure shows that increasing the number of elements, or reducing their size, improves the accuracy of the BEM results. In addition, a time convergence analysis is performed with $\Delta\tau = 0.01,\ 0.001$, and 0.0001 for the thermal stress intensity factor (SIF) distribution along the x_1 axis, as shown in Figure 13. This figure shows that the time step size has a substantial effect on accuracy, with smaller steps generally improving BEM accuracy.

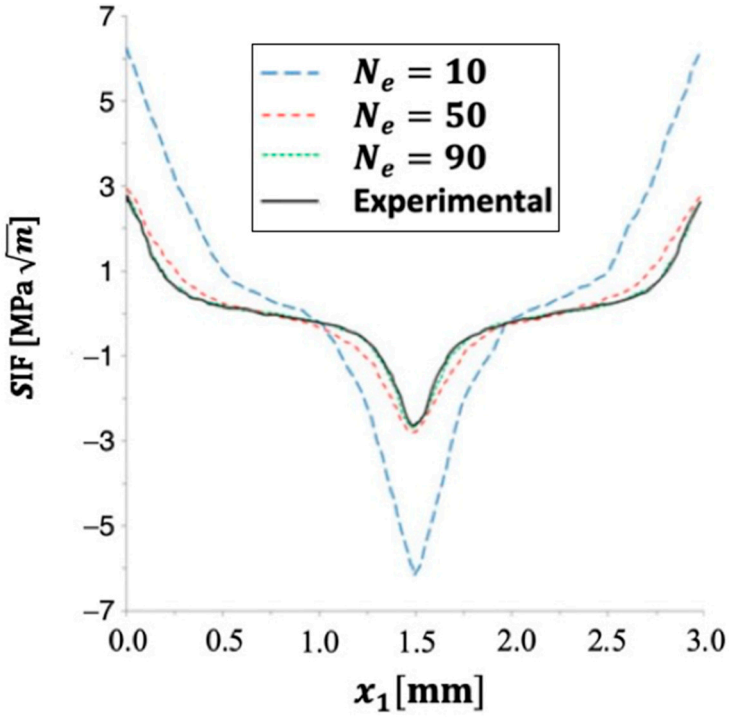

Figure 12. Special-case thermal stress intensity factor (SIF) distribution along x_1 axis for different numbers of elements N_e.

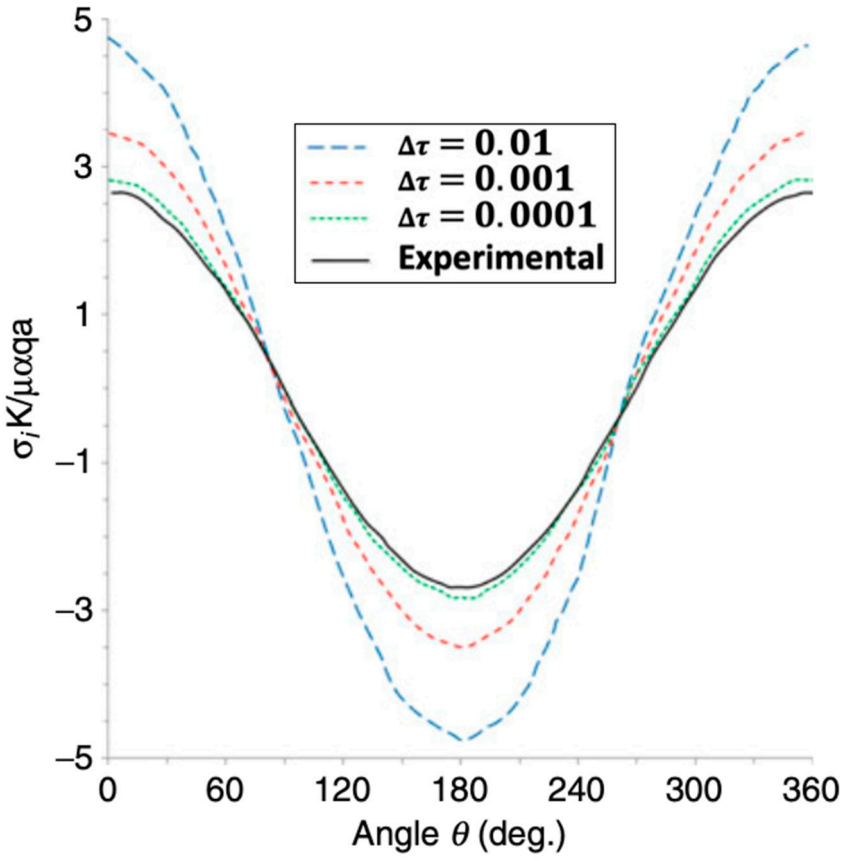

Figure 13. Special-case thermal stress intensity factor (SIF) distribution along x_1 axis for different time step sizes $\Delta\tau$.

7. Conclusions

The analysis of the numerical results allows us to make some final observations:

1. A novel fractional BEM has been developed to address anomalous thermal stress issues in cement-based materials.
2. The suggested formulation determines the unknown values of temperature and heat flux at time τ_{n+1} using their current values and all preceding temperature data.
3. The proposed formulation can overcome the non-locality of the fractional operators.
4. The proposed fractional BEM formulation produces precise and dependable findings; even a modest value of the fractional time derivative, $a = 0.005$, resulted in good agreement with previously reported results. This led us to believe that the fractional BEM formulation can cover the entire range $0 < a \leq 1$.
5. The equality sign in $0 < a \leq 1.0$ is permitted because the conventional thermal stress problem is a specific case of an anomalous thermal stress problem.
6. The proposed Caputo derivative BEM shows that the boundary element technique is a valuable tool for solving fractional and fracture problems in cement-based materials.
7. BEM solves problems more efficiently and accurately than domain techniques, minimizing the processing costs.
8. BEM emerges as the most appropriate solution for the situation under consideration.
9. The versatility of cement-based materials has led to their extensive use throughout human society. Hydraulic binders were adjusted to meet functional requirements in various settings. To safeguard the environment from contamination, cement-based compounds have been used in several sectors, including water and soil. To improve these materials' functionality in a variety of applications,
    I. Consider investigating the effects of incorporating industrial waste into cements, such as ordinary Portland cement (OPC), to increase productivity.
    II. Create models, such as the proposed model, that forecast materials' long-term behavior.
10. Cement-based products have been widely employed in numerous applications, such as bridges, walkways, slabs, pavements, floors, and walls and are among the structural and prefabricated components constructed with cement-based materials. Concrete is also utilized to construct storage tanks, swimming pools, subterranean parking lots, and other structures.
11. Future work on the numerical model will focus on anomalous moisture transport, thermal stress sensitivity assessment, and optimization calculations of elastic and elastic-plastic formulations in cement-based materials, all while lowering operation and maintenance costs.

Author Contributions: Conceptualization, M.A.F.; Methodology, M.A.F.; Software, M.A.F.; Validation, M.A.F.; Formal analysis, M.A.F. and R.A.A.J.; Investigation, M.A.F. and R.A.A.J.; Resources, M.A.F. and R.A.A.J.; Data curation, M.A.F. and R.A.A.J.; Writing—original draft, M.A.F. and R.A.A.J.; Writing—review & editing, M.A.F. and R.A.A.J. All authors have read and agreed to the published version of the manuscript.

Funding: Deanship of Graduate Studies and Scientific Research, Jazan University, Saudi Arabia, through Project Number GSSRD-24.

Data Availability Statement: All data generated or analyzed during this study are included in this published article.

Conflicts of Interest: The authors declare no conflicts of interest.

Nomenclature

a	Fractional-order parameter	D_{x_1} & D_{x_2}	Diffusion coefficients
$\Delta\tau$	Time interval	d	Height of three-point beam
β_{ij}	Stress–temperature coefficients N/K m^2	e	$= \varepsilon_{kk} = \epsilon_{kk}$ Dilatation
δ_{ij}	Kronecker delta $(i,\ j = 1,\ 2)$	$\overline{k}$	Permeability $(\mathrm{m}^4/\mathrm{Ns})$
ε_{ij}	Strain tensor	ℓ	Crack length
ζ	Fluid volume variation (m^3)	$N_{i,o}(t)$	Basis functions of order o
λ	Tractions, Pa	n_{x_1} & n_{x_2}	Unit outward normal components
ξ	$= (\xi_{x_1}, \xi_{x_2})$ Source point	p	Pore pressure, Pa
μ	Shape factor	q	Heat flux
ρ	$= \rho_s(1-\phi) + \phi\rho_{\mathcal{F}}$ Bulk density $(\mathrm{kg}/\mathrm{m}^3)$	q_a	Fluid specific flux
$\rho_{\mathcal{F}}$	Fluid density $(\mathrm{kg}/\mathrm{m}^3)$	R	Solid–fluid coupling parameter
ρ_s	Solid density $(\mathrm{kg}/\mathrm{m}^3)$	$\mathbb{R}$	Domain
σ_{ij}	Total stress tensor, Pa	s_t	Splitting tensile strength of concrete
σ_b	Break point stress	T	Temperature functions, K
σ_c	Cohesive stress	u	Crack opening displacement
τ	Time, s	u_0	Stress-free crack width
ϕ	$= \frac{V^{\mathrm{f}}}{V}$ Porosity	u_i	Solid displacements, m
φ	Interpolation function	u_s	Break point displacement
$\bar{\chi}$ & $\overline{\overline{\chi}}$	Weighting functions	V	$= V^{\mathrm{f}} + V^{\mathrm{s}}$ Bulk volume (m^3)
A	Biot's effective stress coefficient	V^{f}	Fluid volume (m^3)
C_{ijkl}	Constant elastic moduli, GPa	V^{s}	Solid volume (m^3)
$\mathbb{C}$	Boundary	v_i	Fluid–solid displacements
$\overline{\mathbb{C}}$	Source term	$\mathbf{x}$	$= (x_1, x_2)$ Field point

References

1. Sun, H.; Zhang, Y.; Baleanu, D.; Chen, W.; Chen, Y. A new collection of real world applications of fractional calculus in science and engineering. *Commun. Nonlinear Sci. Numer. Simul.* **2018**, *64*, 213–231. [CrossRef]
2. Miller, K.S.; Ross, B. *An Introduction to the Fractional Calculus and Fractional Differential Equations*; Wiley-Interscience: Hoboken, NJ, USA, 1993.
3. Ortigueira, M.D. *Fractional Calculus for Scientists and Engineers*; Lectures Notes in Electrical Engineering; Springer: Berlin/Heidelberg, Germany, 2011; Volume 84.
4. Küntz, M.; Lavallée, P. Experimental evidence and theoretical analysis of anomalous diffusion during water infiltration in porous building materials. *J. Phys. D Appl. Phys.* **2001**, *34*, 2547–2554. [CrossRef]
5. Li, Q.; Xu, S.; Zeng, Q. A fractional kinetic model for drying of cement-based porous materials. *Dry. Technol.* **2015**, *34*, 1231–1242. [CrossRef]
6. Alderete, N.; Zaccardi, Y.V.; De Belie, N. Physical evidence of swelling as the cause of anomalous capillary water uptake by cementitious materials. *Cem. Concr. Res.* **2019**, *120*, 256–266. [CrossRef]
7. Srimook, P.; Maruyama, I. Anomalous moisture transport in dried cementitious material: A numerical analysis. *Constr. Build. Mater.* **2024**, *449*, 138365. [CrossRef]
8. Zhang, L.; Ren, Q.; Li, Z.; Zhang, G. Predicting the Drying of Concrete by an Anomalous Diffusion Model. *J. Mater. Civ. Eng.* **2019**, *31*, 04019010. [CrossRef]
9. Chen, W.; Sun, H.; Zhang, X.; Korošak, D. Anomalous diffusion modeling by fractal and fractional derivatives. *Comput. Math. Appl.* **2010**, *59*, 1754–1758. [CrossRef]
10. A. Lockington, D.; Parlange, J.-Y. Anomalous water absorption in porous materials. *J. Phys. D Appl. Phys.* **2003**, *36*, 760–767. [CrossRef]
11. Taylor, S.C.; Hoff, W.D.; Wilson, M.A.; Green, K.M. Anomalous water transport properties of Portland and blended cement-based materials. *J. Mater. Sci. Lett.* **1999**, *18*, 1925–1927. [CrossRef]
12. Saeidpour, M.; Wadsö, L. Evidence for anomalous water vapor sorption kinetics in cement based materials. *Cem. Concr. Res.* **2015**, *70*, 60–66. [CrossRef]
13. Zhang, Z.; Angst, U. Modelling Anomalous Moisture Transport in Cement-Based Materials by the Dual-Permeability Concept. *Int. J. Mol. Sci.* **2020**, *21*, 837. [CrossRef]
14. Coussy, O. *Mechanics of Porous Continua*; John Wiley and Sons Ltd.: Chichester, UK, 1995.
15. Mainguy, M.; Coussy, O.; Baroghel-Bouny, V. Role of Air Pressure in Drying of Weakly Permeable Materials. *J. Eng. Mech.* **2001**, *127*, 582–592. [CrossRef]
16. Philip, J.R.; De Vries, D.A. Moisture movement in porous materials under temperature gradients. *Trans. Am. Geophys. Union* **1957**, *38*, 222–232. [CrossRef]

17. Zhang, Z.; Thiery, M.; Baroghel-Bouny, V. An equation of drying kinetics for cementitious materials. *Dry. Technol.* **2017**, *36*, 1446–1459. [CrossRef]
18. Lockington, D.; Parlange, J.-Y.; Dux, P. Sorptivity and the estimation of water penetration into unsaturated concrete. *Mater. Struct.* **1999**, *32*, 342–347. [CrossRef]
19. Mindess, S.; Young, J.F. *Concrete*; Prentice-Hall: Englewood Cliffs, NJ, USA, 1983.
20. Zeng, Q.; Xu, S. A two-parameter stretched exponential function for dynamic water vapor sorption of cement-based porous materials. *Mater. Struct.* **2017**, *50*, 128. [CrossRef]
21. Scherer, G.W. Drying, Shrinkage, and Cracking of Cementitious Materials. *Transp. Porous Media* **2015**, *110*, 311–331. [CrossRef]
22. Zhou, C.; Ren, F.; Wang, Z.; Chen, W.; Wang, W. Why Permeability to Water Is Anomalously Lower than That to Many Other Fluids for Cement-Based Material? *Cem. Concr. Res.* **2017**, *100*, 373–384. [CrossRef]
23. Wang, L.; Hoyos, L.R.; Wang, J.; Voyiadjis, G.; Abadie, C. Anisotropic Properties of Asphalt Concrete: Characterization and Implications for Pavement Design and Analysis. *J. Mater. Civ. Eng.* **2005**, *17*, 535–543. [CrossRef]
24. Maruyama, I.; Rymeš, J.; Vandamme, M.; Coasne, B. Cavitation of water in hardened cement paste under short-term desorption measurements. *Mater. Struct.* **2018**, *51*, 159. [CrossRef]
25. Zhang, Z.; Thiery, M.; Baroghel-Bouny, V. Investigation of moisture transport properties of cementitious materials. *Cem. Concr. Res.* **2016**, *89*, 257–268. [CrossRef]
26. Xi, Y.; Bažant, Z.P.; Molina, L.; Jennings, H.M. Moisture diffusion in cementitious materials Moisture capacity and diffusivity. *Adv. Cem. Based Mater.* **1994**, *1*, 258–266. [CrossRef]
27. Baroghel-Bouny, V. Water vapour sorption experiments on hardened cementitious materials. Part II: Essential tool for assessment of transport properties and for durability prediction. *Cem. Concr. Res.* **2007**, *37*, 438–454. [CrossRef]
28. Savage, B.M.; Janssen, D.J. Soil Physics Principles Validated for Use in Predicting Unsaturated Moisture Movement in Portland Cement Concrete. *ACI Mater. J.* **1997**, *94*, 63–70.
29. Monlouis-Bonnaire, J.; Verdier, J.; Perrin, B. Prediction of the relative permeability to gas flow of cement-based materials. *Cem. Concr. Res.* **2004**, *34*, 737–744. [CrossRef]
30. Zhou, C. Predicting water permeability and relative gas permeability of unsaturated cement-based material from hydraulic diffusivity. *Cem. Concr. Res.* **2014**, *58*, 143–151. [CrossRef]
31. Carlier, J.-P.; Burlion, N. Experimental and Numerical Assessment of the Hydrodynamical Properties of Cementitious Materials. *Transp. Porous Media* **2010**, *86*, 87–102. [CrossRef]
32. Zhang, Z.; Thiery, M.; Baroghel-Bouny, V. Numerical modelling of moisture transfers with hysteresis within cementitious materials: Verification and investigation of the effects of repeated wetting–drying boundary conditions. *Cem. Concr. Res.* **2015**, *68*, 10–23. [CrossRef]
33. Zhang, Z.; Thiéry, M.; Baroghel-Bouny, V. A review and statistical study of existing hysteresis models for cementitious materials. *Cem. Concr. Res.* **2014**, *57*, 44–60. [CrossRef]
34. Carlier, J.-P.; Rougelot, T.; Burlion, N. Performance evaluation of models describing sorption isotherm in cementitious materials between saturation and oven dryness. *Constr. Build. Mater.* **2012**, *37*, 58–66. [CrossRef]
35. Jonasson, J.E.; Growth, P.; Hedlund, H. Modelling of temperature and moisture field in concrete to study early ages movements as a basis for stress analysis. In *Thermal Cracking in Concrete at Early Ages, Proceedings RILEM Symposium, Munich*; CRC Press: Boca Raton, FL, USA, 1994; pp. 45–52.
36. Honorio, T.; Bary, B.; Benboudjema, F. Thermal properties of cement-based materials: Multiscale estimations at early-age. *Cement and Concrete Composites* **2018**, *87*, 205–219. [CrossRef]
37. Lee, S.L.; Tam, C.T.; Swaddiwudhipong, S.; Mani, A.C. Temperature distribution and thermal stresses in thick concrete pours. In Proceedings of the 3rd International Conference on Structural Failure, Singapore, 23–26 July 1991; pp. 17–33.
38. Ceretani, A.N. A Note on Models for Anomalous Phase-Change Processes. *Fract. Calc. Appl. Anal.* **2020**, *23*, 167–182. [CrossRef]
39. Patnaik, S.; Sidhardh, S.; Semperlotti, F. A Ritz-based finite element method for a fractional-order boundary value problem of nonlocal elasticity. *Int. J. Solids Struct.* **2020**, *202*, 398–417. [CrossRef]
40. Fahmy, M.A. BEM Modeling for Stress Sensitivity of Nonlocal Thermo-Elasto-Plastic Damage Problems. *Computation* **2024**, *12*, 87. [CrossRef]
41. Brebbia, C.A.; Telles, J.C.F.; Wrobel, L.C.; Mukherjee, S. Boundary Element Techniques. Theory and Applications in Engineering. *J. Appl. Mech.* **1985**, *52*, 241. [CrossRef]
42. Katsikadelis, J.T. The BEM for numerical solution of partial fractional differential equations. *Comput. Math. Appl.* **2011**, *62*, 891–901. [CrossRef]
43. Dehghan, M.; Safarpoor, M. The dual reciprocity boundary elements method for the linear and nonlinear two-dimensional time-fractional partial differential equations. *Math. Methods Appl. Sci.* **2016**, *39*, 3979–3995. [CrossRef]
44. Carrer, J.A.M.; Seaid, M.; Trevelyan, J.; Solheid, B.d.S. The boundary element method applied to the solution of the anomalous diffusion problem. *Eng. Anal. Bound. Elements* **2019**, *109*, 129–142. [CrossRef]
45. Fahmy, M.A. Fractional Temperature-Dependent BEM for Laser Ultrasonic Thermoelastic Propagation Problems of Smart Nanomaterials. *Fractal Fract.* **2023**, *7*, 536. [CrossRef]
46. Fahmy, M.A.; Alsulami, M.O.; Abouelregal, A.E. Three-Temperature Boundary Element Modeling of Ultrasound Wave Propagation in Anisotropic Viscoelastic Porous Media. *Axioms* **2023**, *12*, 473. [CrossRef]

47. Fahmy, M.A. Boundary Element Algorithm for Modeling and Simulation of Dual-Phase Lag Bioheat Transfer and Biomechanics of Anisotropic Soft Tissues. *Int. J. Appl. Mech.* **2018**, *10*, 1850108. [CrossRef]
48. Fahmy, M.A.; Alsulami, M.O.; Abouelregal, A.E. Sensitivity analysis and design optimization of 3T rotating thermoelastic structures using IGBEM. *AIMS Math.* **2022**, *7*, 19902–19921. [CrossRef]
49. Fahmy, M.A. Boundary Element Algorithm for Nonlinear Modeling and Simulation of Three-Temperature Anisotropic Generalized Micropolar Piezothermoelasticity with Memory-Dependent Derivative. *Int. J. Appl. Mech.* **2020**, *12*, 2050027. [CrossRef]
50. Fahmy, M.A.; Alzubaidi, M.H.M. A boundary element analysis of quasi-potential inviscid incompressible flow in multiply connected airfoil wing. *J. Umm Al-Qura Univ. Eng. Arch.* **2024**, *15*, 398–402. [CrossRef]
51. Fahmy, M.A. A time-stepping DRBEM for nonlinear fractional sub-diffusion bio-heat ultrasonic wave propagation problems during electromagnetic radiation. *J. Umm Al-Qura Univ. Appl. Sci.* **2024**. [CrossRef]
52. Fahmy, M.A.; Toujani, M. Fractional Boundary Element Solution for Nonlinear Nonlocal Thermoelastic Problems of Anisotropic Fibrous Polymer Nanomaterials. *Computation* **2024**, *12*, 117. [CrossRef]
53. Fahmy, M.A. Design optimization for a simulation of rotating anisotropic viscoelastic porous structures using time-domain OQBEM. *Math. Comput. Simul.* **2019**, *166*, 193–205. [CrossRef]
54. Fahmy, M.A.; Shaw, S.; Mondal, S.; Abouelregal, A.E.; Lotfy, K.; Kudinov, I.A.; Soliman, A.H. Boundary Element Modeling for Simulation and Optimization of Three-Temperature Anisotropic Micropolar Magneto-thermoviscoelastic Problems in Porous Smart Structures Using NURBS and Genetic Algorithm. *Int. J. Thermophys.* **2021**, *42*, 29. [CrossRef]
55. Brebbia, C.A.; Dominguez, J. *Boundary Elements: An Introductory Course*; WIT Press & Computational Mechanics Publication: Boston, MA, USA; Southampton, UK, 1998.
56. Zienkiewicz, O.C.; Morgan, K. *Finite Elements & Approximation*; John Wiley & Sons, Inc.: New York, NY, USA, 1983.
57. Carrer, J.A.M.; Cunha, C.L.N.; Mansur, W.J. The boundary element method applied to the solution of two-dimensional diffusion–advection problems for non-isotropic materials. *J. Braz. Soc. Mech. Sci. Eng.* **2017**, *39*, 4533–4545. [CrossRef]
58. Berger, J.R.; Karageorghis, A. The Method of Fundamental Solutions for Heat Conduction in Layered Materials. *Int. J. Numer. Methods Eng.* **1999**, *45*, 1681–1694. [CrossRef]
59. Carrer, J.; Solheid, B.; Trevelyan, J.; Seaid, M. A boundary element method formulation based on the Caputo derivative for the solution of the anomalous diffusion problem. *Eng. Anal. Bound. Elements* **2021**, *122*, 132–144. [CrossRef]
60. Huang, F.-Y.; Liang, K.-Z. Boundary element method for micropolar thermoelasticity. *Eng. Anal. Bound. Elements* **1996**, *17*, 19–26. [CrossRef]
61. Eringen, A.C. Theory of Micropolar Elasticity. In *Fracture*; Liebowitz, H., Ed.; Academic Press: New York, NY, USA, 1968; pp. 621–729.
62. Dragos, L. Fundamental solutions in micropolar elasticity. *Int. J. Eng. Sci.* **1984**, *22*, 265–275. [CrossRef]
63. Salama, F.M.; Hamid, N.N.A.; Ali, N.H.M.; Ali, U. An efficient modified hybrid explicit group iterative method for the time-fractional diffusion equation in two space dimensions. *AIMS Math.* **2022**, *7*, 2370–2392. [CrossRef]
64. Dong, W.; Wu, Z.; Zhou, X.; Wang, C. A comparative study on two stress intensity factor-based criteria for prediction of mode-I crack propagation in concrete. *Eng. Fract. Mech.* **2016**, *158*, 39–58. [CrossRef]
65. Petersson, P.E. *Crack Growth and Development of Fracture Zones in Plain Concrete and Similar Materials*; Division of Building Materials, LTH, Lund University: Lund, Sweden, 1981; Volume 1006.
66. Jenq, Y.; Shah, S. A Fracture toughness criterion for concrete. *Eng. Fract. Mech.* **1985**, *21*, 1055–1069. [CrossRef]
67. Cifuentes, H.; Montero-Chacón, F.; Galán, J.; Cabezas, J.; la Concha, A.M.-D. A Finite Element-Based Methodology for the Thermo-mechanical Analysis of Early Age Behavior in Concrete Structures. *Int. J. Concr. Struct. Mater.* **2019**, *13*, 41. [CrossRef]
68. RILEM TCS. Determination of the fracture energy of mortar and concrete by means of three-point bend tests on notched beams. *Mater. Struct.* **1985**, *18*, 287–290. [CrossRef]
69. Do, T.A. A Combination of Finite Difference and Finite Element Methods for Temperature and Stress Predictions of Early-Age Concrete Members. In *Finite Element Methods and Their Applications*; Baccouch, M., Ed.; IntechOpen: London, UK. [CrossRef]
70. Lin, Y.; Chen, H.-L. Thermal analysis, and adiabatic calorimetry for early-age concrete members. *J. Therm. Anal. Calorim.* **2016**, *124*, 227–239. [CrossRef]
71. Darvishi, M.; Hessari, P. A modified symmetric successive overrelaxation method for augmented systems. *Comput. Math. Appl.* **2011**, *61*, 3128–3135. [CrossRef]
72. Hadjidirnos, A.; Psimarni, A.; Saridakis, Y.G.; Yeyios, A.K. *The Block Modified Accelerated Overrelaxation (MAOR) Method for Generalized Consistently Ordered Matrices*; Department of Computer Science Technical Reports; Paper 23; Purdue University: West Lafayette, IN, USA, 1990. Available online: %20https://docs.lib.purdue.edu/cstech/23 (accessed on 18 December 2024).